JACS
JOURNAL OF THE AMERICAN CHEMICAL SOCIETY
pubs.acs.org/JACS
Article

Introducing Hydrogen-Bonding Microenvironment in Close Proximity to Single-Atom Sites for Boosting Photocatalytic Hydrogen Production

Shuaishuai Hu, Ming-Liang Gao, Jiajia Huang, He Wang, Qingyu Wang, Weijie Yang, Zhihu Sun, Xusheng Zheng, and Hai-Long Jiang*

Cite This: J. Am. Chem. Soc. 2024, 146, 20391−20400

Read Online

ACCESS | Metrics & More | Article Recommendations | Supporting Information

ABSTRACT: Inspired by enzymatic catalysis, it is crucial to construct hydrogen-bonding-rich microenvironment around catalytic sites; unfortunately, its precise construction and understanding how the distance between such microenvironment and catalytic sites affects the catalysis remain significantly challenging. In this work, a series of metal−organic framework (MOF)-based single-atom Ru_1 catalysts, namely, Ru_1/UiO-67-X (X = -H, -*m*-$(NH_2)_2$, -*o*-$(NH_2)_2$), have been synthesized, where the distance between the hydrogen-bonding microenvironment and Ru_1 sites is modulated by altering the location of amino groups. The $-NH_2$ group can form hydrogen bonds with H_2O, constituting a unique microenvironment that causes an increased water concentration around the Ru_1 sites. Remarkably, Ru_1/UiO-67-*o*-$(NH_2)_2$ displays a superior photocatalytic hydrogen production rate, ∼4.6 and ∼146.6 times of Ru_1/UiO-67-*m*-$(NH_2)_2$ and Ru_1/UiO-67, respectively. Both experimental and computational results suggest that the close proximity of amino groups to the Ru_1 sites in Ru_1/UiO-67-*o*-$(NH_2)_2$ improves charge transfer and H_2O dissociation, accounting for the promoted photocatalytic hydrogen production.

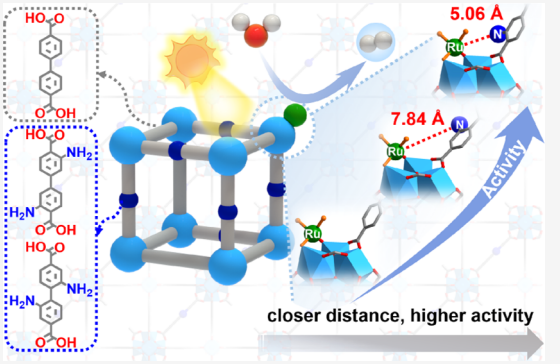

INTRODUCTION

Hydrogen energy is deemed one of the eco-friendly and sustainable alternatives to fossil fuels due to its renewable, clean, and high-efficiency features.[1,2] The photocatalytic hydrogen production technology attracts widespread attention, resulting from the direct conversion of solar energy into hydrogen energy.[3−5] The technology mimics natural photosynthesis, aiming at high-efficiency and low-cost hydrogen production.[3−5] To achieve this goal, a variety of strategies have been developed, such as introducing cocatalysts, creating structural defects, tailoring the morphology and composition of catalysts, and so on.[6−12] Despite related progress showing great promise, the efficiency of photocatalytic hydrogen production remains a formidable challenge toward practical application.

Inspired by the ideal catalytic performance of enzymes in biochemical reactions, the noncovalent interaction microenvironment formed by substrates and amino acid residues within the binding pocket, surrounding catalytic centers, plays crucial roles in enriching, organizing, and activating substrates,[13,14] which might be worth learning for improving the activity in photocatalytic hydrogen production. However, the introduction of a noncovalent interaction in traditional heterogeneous catalysts is difficult, given the challenge in their structural regulation. While the distance between catalytic sites and the substrate, directed by the weak interaction, might be critical for the resulting photocatalytic performance, this remains basically unknown in literatures. To construct a suitable photocatalyst platform with a controlled distance between the catalytic site and its adjacent noncovalent interaction site for substrates, the precise location and regulation of both sites are highly desired. In this context, it is of great importance to find suitable supports with well-defined and readily modifiable structures, so that the above two sites can be accurately installed to the specific locations.

Considering the aforementioned requirement, metal−organic frameworks (MOFs), a class of crystalline porous materials, stand out due to their atomically precise and highly tailorable structures.[15−21] These unique advantages make MOFs ideal platforms for structural design and modification; moreover, MOFs have been demonstrated to have great potential in photocatalytic hydrogen production.[22−26] Recently, the metal clusters within MOFs have been demon-

Received: May 2, 2024
Revised: June 28, 2024
Accepted: July 3, 2024
Published: July 10, 2024

https://doi.org/10.1021/jacs.4c06013
J. Am. Chem. Soc. 2024, 146, 20391−20400

Scheme 1. Illustration Showing the Synthetic Strategy for Ru_1/UiO-67-X (X = -H, -*m*-$(NH_2)_2$, -*o*-$(NH_2)_2$)

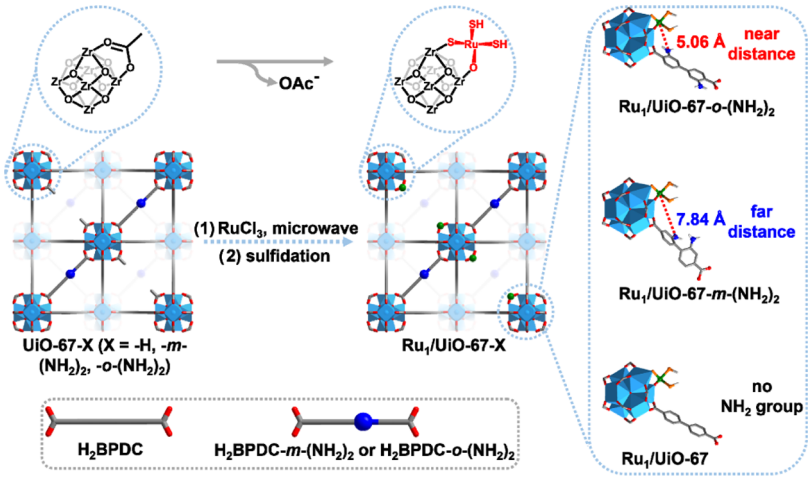

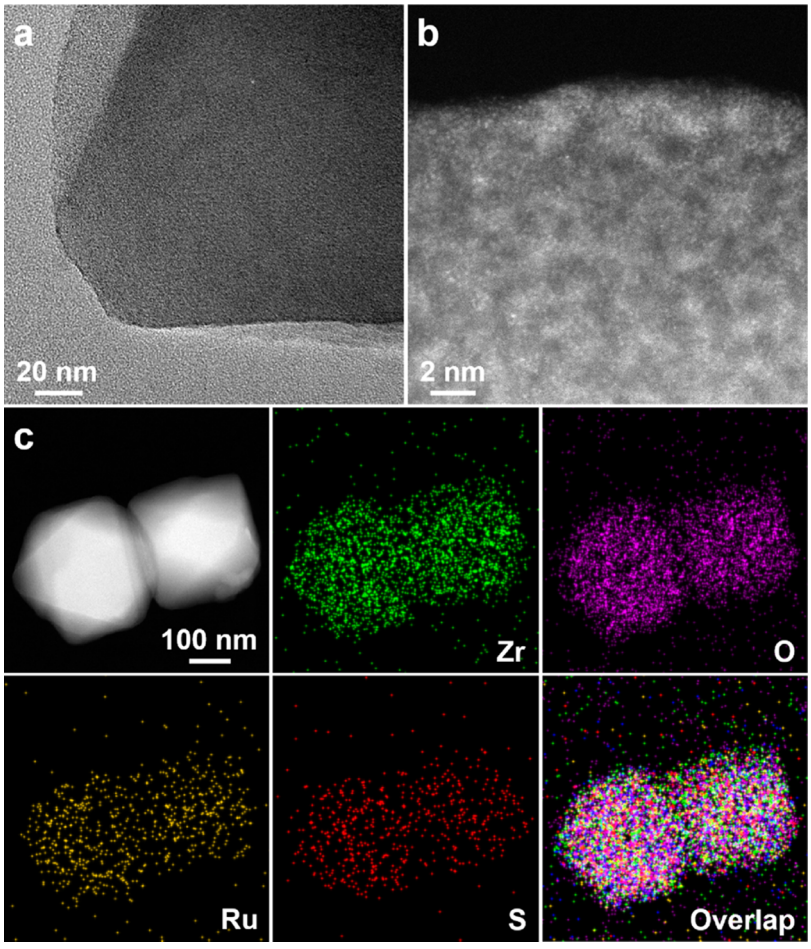

Figure 1. (a) TEM and (b) aberration-corrected HAADF-STEM images of Ru_1/UiO-67-*o*-$(NH_2)_2$. (c) HAADF-STEM image of Ru_1/UiO-67-*o*-$(NH_2)_2$ and the corresponding EDS elemental mapping images for Zr, O, Ru, S, and their overlap.

strated to be promising supports for anchoring single metal atoms with clear locations.[27−31] In addition, the functional groups for the noncovalent interaction can be furnished on the organic linkers and the group type and location are adjustable.[32] Despite this, to our knowledge, regulating the distance between the catalytic site and the noncovalent interaction site (for inducing substrates) in heterogeneous catalysts is yet to be reported.

In this work, single Ru_1 atoms are precisely anchored onto Zr-oxo clusters in UiO-67-X (X = -H, -*m*-$(NH_2)_2$, -*o*-$(NH_2)_2$), resulting in the synthesis of Ru_1/UiO-67-X for photocatalytic hydrogen production. The crystalline and porous structure of the MOF allows the Ru_1 sites to be well dispersed and improves their accessibility for subsequent catalysis. The hydrogen-bonding microenvironment around Ru_1 sites is created based on the $-NH_2$ group that can form hydrogen

https://doi.org/10.1021/jacs.4c06013
J. Am. Chem. Soc. 2024, 146, 20391−20400

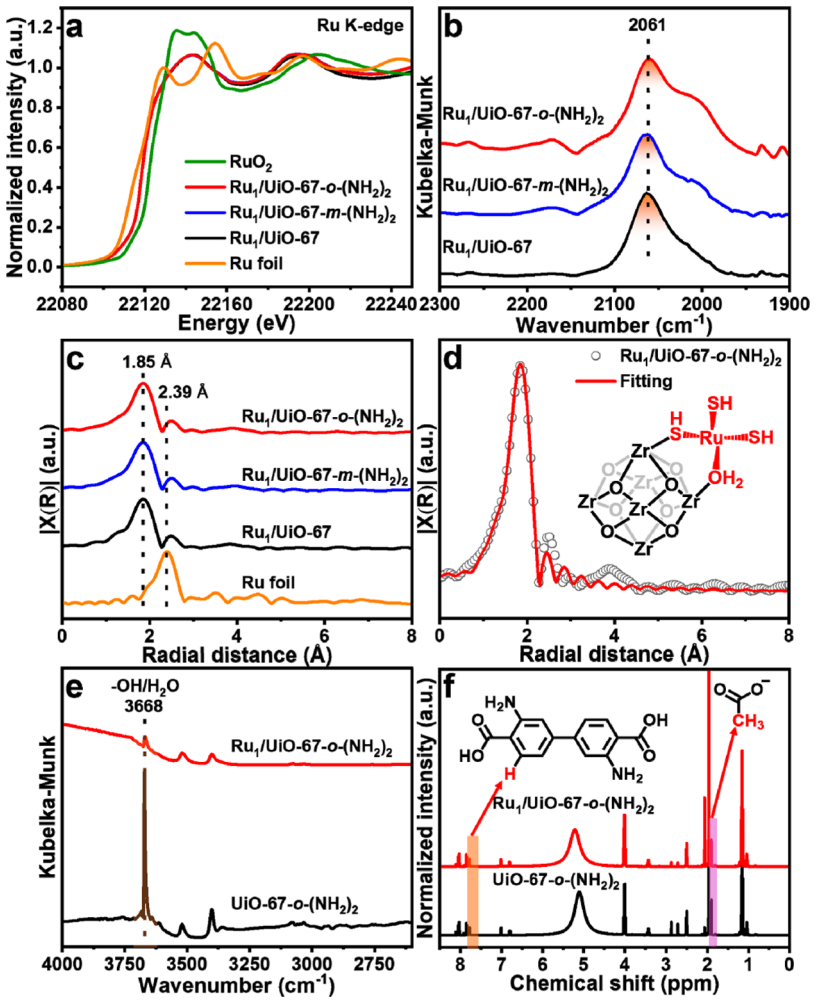

Figure 2. (a) Ru K-edge XANES spectra for Ru_1/UiO-67-X, with the Ru foil and RuO_2 serving as reference materials. (b) CO−DRIFTS spectra of Ru_1/UiO-67-X. (c) FT-EXAFS spectra of Ru_1/UiO-67-X and the Ru foil. (d) EXAFS fitting curve of Ru_1/UiO-67-*o*-$(NH_2)_2$ (inset: the proposed coordination structure of the single Ru atom anchored on the Zr-oxo cluster). (e) DRIFTS spectra and (f) ^{1}H NMR spectra of UiO-67-*o*-$(NH_2)_2$ and Ru_1/UiO-67-*o*-$(NH_2)_2$.

bonding with H_2O molecules. Moreover, the distance between Ru_1 sites and the $-NH_2$ group (the site interacting with H_2O) can be readily controlled by altering the location of amino groups on the linker (Scheme 1). Remarkably, Ru_1/UiO-67-*o*-$(NH_2)_2$ featuring hydrogen-bonding microenvironment in close proximity to Ru_1 sites showcases a very high activity of 20.52 mmol g^{-1} h^{-1}, which is ∼4.6 and ∼146.6 times higher than that of Ru_1/UiO-67-*m*-$(NH_2)_2$ and Ru_1/UiO-67, respectively. Results indicate that the hydrogen-bonding microenvironment and its proximity around the Ru_1 sites are crucial for the photocatalytic activity. This finding provides an innovative strategy toward enhanced photocatalysis.

RESULTS AND DISCUSSION

UiO-67, a representative MOF, was synthesized using 4,4′-biphenyldicarboxylic acid (H_2BPDC) and $ZrCl_4$ under solvothermal conditions.[33,34] Isoreticular UiO-67-*m*-$(NH_2)_2$ and UiO-67-*o*-$(NH_2)_2$ (different distances between the amino and carboxylic groups in these two MOFs) were produced using a mixed-linker strategy under similar conditions. The molar ratio of H_2BPDC to H_2BPDC-*m*-$(NH_2)_2$ (2,2′-diamino-1,1′-biphenyl-4,4′-dicarboxylic acid) or H_2BPDC-*o*-$(NH_2)_2$ (3,3′-diamino-1,1′-biphenyl-4,4′-dicarboxylic acid) was 1:1 in the corresponding MOFs, as confirmed by ^{1}H NMR spectra (Figures S1 and S2). The Ru^{3+} ions were introduced to UiO-67-X (X = -H, -*m*-$(NH_2)_2$, -*o*-$(NH_2)_2$) by a microwave-assisted synthetic approach (uncoordinated −OH/H_2O groups on the Zr-oxo clusters of UiO-67-X capable of anchoring the Ru_1 sites),[30] followed by sulfidation using thioacetamide (for modulating the coordination environment and electronic structure of Ru_1 sites),[30] yielding Ru_1/UiO-67-X with similar Ru loadings of ∼1.1 wt %, determined by inductively coupled plasma atomic emission spectroscopy (ICP-AES) analysis (Table S1). Powder X-ray diffraction (XRD) patterns suggest that the crystallinity of parent UiO-67-X remains after the anchoring of Ru species (Figure S3). Brunauer−Emmet−Teller (BET) surface areas of Ru_1/UiO-67-X show a slight decrease to the parent MOF, possibly due to the mass occupancy of Ru sites (Figure S4).[35] Scanning electron microscopy (SEM) images indicate that all Ru_1/UiO-67-X present a similar octahedral morphology to the parent MOFs (Figure S5). The Ru nanoparticle is not generated in Ru_1/UiO-67-X from the transmission electron microscopy (TEM) observation (Figures 1a and S6). Aberration-corrected high-angle annular dark-field scanning transmission electron microscopy (HAADF-STEM) images of Ru_1/UiO-67-*o*-

https://doi.org/10.1021/jacs.4c06013
J. Am. Chem. Soc. 2024, 146, 20391−20400

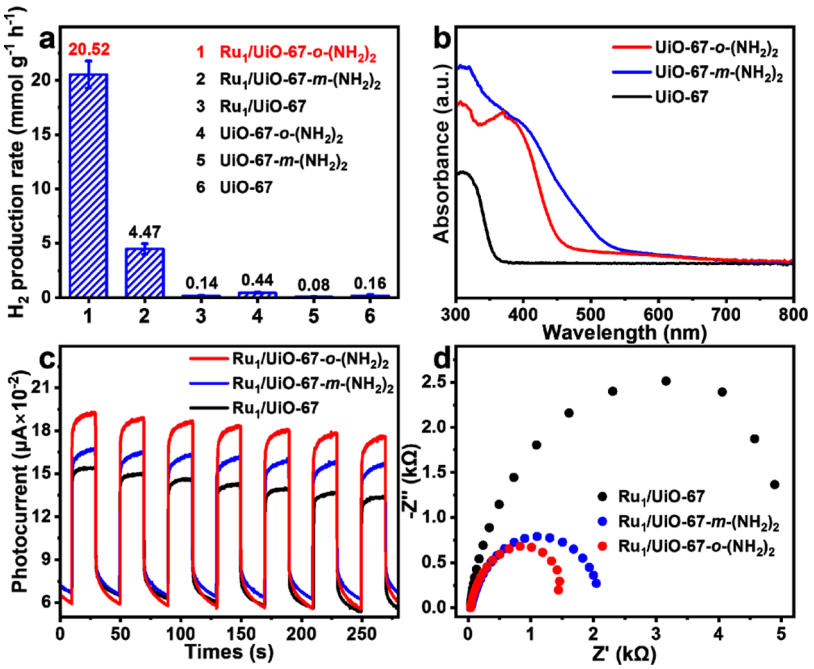

Figure 3. (a) Photocatalytic hydrogen production rates of Ru_1/UiO-67-X and UiO-67-X for 1 h. Reaction conditions: 5 mg of the catalyst, 18 mL of acetonitrile, 2 mL of TEA, 0.2 mL of H_2O, and $\lambda > 380$ nm. (b) UV−vis spectra of UiO-67-X. (c) Photocurrent responses of Ru_1/UiO-67-X. (d) EIS Nyquist plots of Ru_1/UiO-67-X.

$(NH_2)_2$ display bright spots, suggesting dense atomic sites (Figures 1b and S7).[36−38] Given the close atomic numbers of Ru and Zr in the composite, it is very difficult to make this distinction. However, the absence of observable nanoparticles implies that single-atom Ru might exist in Ru_1/UiO-67-*o*-$(NH_2)_2$.[36] The HAADF-STEM image and the corresponding energy-dispersive X-ray spectroscopy (EDS) elemental mapping images of Ru_1/UiO-67-X jointly demonstrate that Ru species is well dispersed throughout the MOF particle (Figures 1c, S8 and S9).

To unveil the detailed information on Ru species in Ru_1/UiO-67-X, X-ray absorption spectroscopy (XAS) analysis has been performed. X-ray absorption near-edge spectroscopy (XANES) shows that the absorption edge of Ru_1/UiO-67-X is positioned between that of the Ru foil and RuO_2, implying that the oxidation states of $Ru^{\delta+}$ species are in the range from 0 to +4 (Figure 2a).[36−38] X-ray photoelectron spectroscopy (XPS) spectra of Ru 3p for Ru_1/UiO-67-X present very similar binding energies at ∼461.9 eV (Figure S10), and the diffuse reflectance infrared Fourier transform spectroscopy (DRIFTS) spectra for CO adsorption on Ru_1/UiO-67-X display a prominent peak at ∼2061 cm^{-1} (Figure 2b). All above results confirm that the Ru species in Ru_1/UiO-67-X possess similar oxidation states. The absence of the Ru−Ru bond (2.39 Å) and the presence of the Ru−S bond (1.85 Å) observed from the Fourier transform extended X-ray absorption fine structure (EXAFS) spectra indicate the formation of single Ru_1 atoms in Ru_1/UiO-67-X (Figure 2c). Subsequent fitting curves reveal that single-atom Ru_1 in Ru_1/UiO-67-X adopts a tetrahedral coordination, bonded to one O and three S atoms (Figures 2d, S11 and Table S2). The XPS spectra of S 2p confirm that the valence state of sulfur species in Ru_1/UiO-67-X is mainly −2 (Figure S12), supporting the −SH coordination around the Ru center. Furthermore, a comparison of the CO−DRIFTS spectra for Ru_1/UiO-67-*o*-$(NH_2)_2$ and Ru_{NPs}/UiO-67-*o*-$(NH_2)_2$ (NPs: nanoparticles) showcases significant differences (Figure S13), further supporting the presence of single Ru_1 atoms in the former.[36] The remarkable intensity reduction of the peak at 3668 cm^{-1}, assignable to the stretching vibration of −OH/H_2O on Zr-oxo clusters, suggests that single Ru_1 atoms interact with the −OH/H_2O groups, as observed in DRIFTS spectra, confirming that the single Ru_1 atoms are precisely anchored onto the Zr-oxo clusters in UiO-67-*o*-$(NH_2)_2$ (Figures 2e and S14).[30] Furthermore, the vibrational peak of the $-NH_2$ group does not shift after anchoring the single Ru atom, so it can be excluded that the single Ru atom is anchored to the $-NH_2$ group (Figure S15). The molar ratios of H_2BPDC-*o*-$(NH_2)_2$:OAc^- for UiO-67-*o*-$(NH_2)_2$ and Ru_1/UiO-67-*o*-$(NH_2)_2$ are 1:1.08 and 1:0.85, respectively, based on the ^{1}H NMR results (Figure 2f). The decrease in the OAc^- content further supports that the OAc^- groups in UiO-67-*o*-$(NH_2)_2$ are replaced by single Ru_1 atoms in Ru_1/UiO-67-*o*-$(NH_2)_2$.[30] Similar findings can also be observed for Ru_1/UiO-67 and Ru_1/UiO-67-*m*-$(NH_2)_2$ (Figures S16 and S17). The above results unambiguously demonstrate that single Ru_1 atoms are precisely anchored onto the Zr-oxo clusters in all Ru_1/UiO-67-X. With a fixed location of catalytic Ru_1 sites and the absence or presence of the amino group (for creating hydrogen-bonding microenvironment) situated at changing locations on the linker, Ru_1/UiO-67-X can be adopted as ideal models for studying the influence of the hydrogen-bonding microenvironment on photocatalysis.

Motivated by the above results, photocatalytic hydrogen production for water splitting over Ru_1/UiO-67-X has been investigated, under visible light irradiation and optimized reaction conditions (Figure S18). Strikingly, the photocatalytic hydrogen production of Ru_1/UiO-67-X exhibits distinctly different rates, featuring the highest activity of 20.52 mmol g^{-1} h^{-1} for Ru_1/UiO-67-*o*-$(NH_2)_2$, while exhibiting markedly lower rates of 4.47 and 0.14 mmol g^{-1} h^{-1} for Ru_1/UiO-67-*m*-$(NH_2)_2$ and Ru_1/UiO-67, respectively, under identical reaction conditions (Figures 3a and S19). The apparent quantum

https://doi.org/10.1021/jacs.4c06013
J. Am. Chem. Soc. 2024, 146, 20391−20400

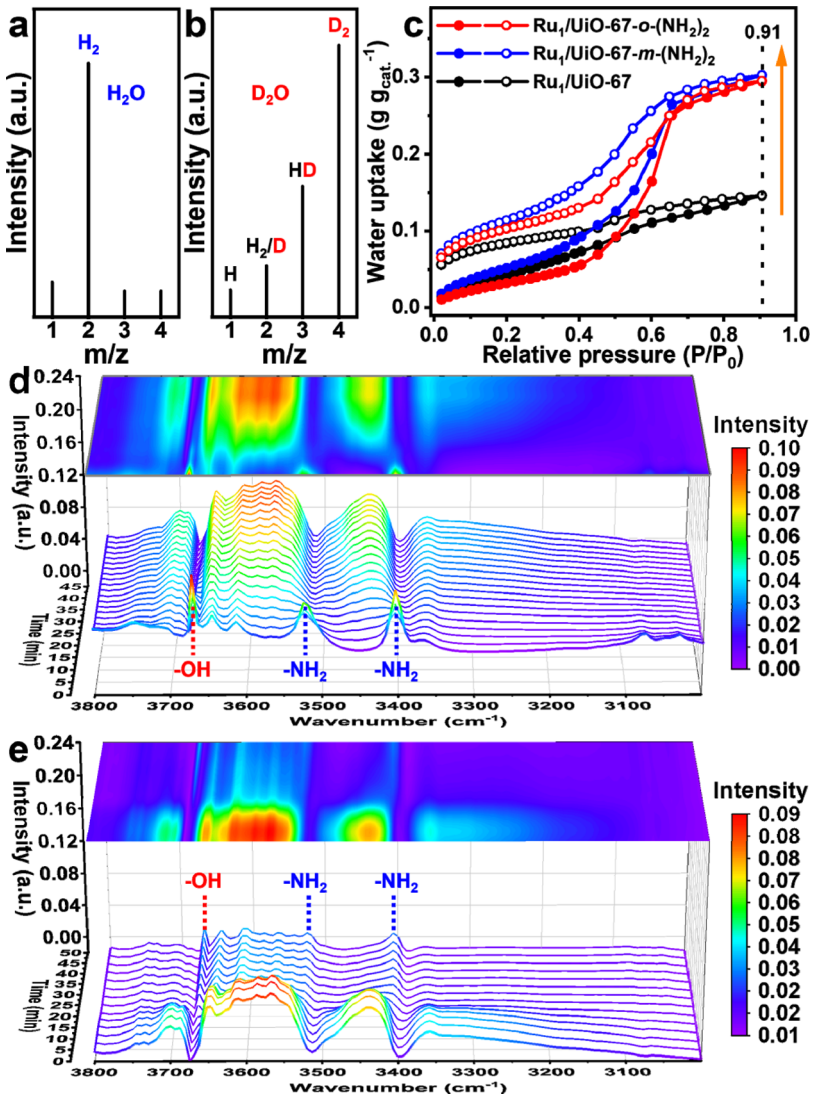

Figure 4. MS spectra of the hydrogen product with (a) H_2O and (b) D_2O as the source of hydrogen. (c) Water vapor adsorption isotherms of Ru_1/UiO-67-X at 298 K. Time-dependent DRIFTS spectra recording (d) water adsorption on UiO-67-*o*-$(NH_2)_2$ and (e) water desorption by purging with Ar gas after water adsorption saturation.

efficiency of Ru_1/UiO-67-*o*-$(NH_2)_2$ at 380 nm is 0.44%. Moreover, it is observed that the photocatalytic hydrogen production rate in Ru_1/UiO-67-*o*-$(NH_2)_2$ significantly varies when the molar ratio of H_2BPDC to H_2BPDC-*o*-$(NH_2)_2$ in the MOF is altered (Figure S20). Obviously, the amino groups contribute to improving the hydrogen production efficiency; meanwhile, the distance between the Ru_1 sites and amino groups is another critical parameter for the activity. To manifest this assumption, the photocatalytic reactions have been conducted with altered amounts of water and types of sacrificial agents; to our delight, a similar activity difference can be observed (Figures S21 and S22).

Moreover, the hydrogen production rates for UiO-67-X are generally very low (Figure 3a), revealing that the single Ru_1 atoms are the real active sites in photocatalytic hydrogen production by water splitting. Photocatalytic recycling experiments for Ru_1/UiO-67-*o*-$(NH_2)_2$ show that no noticeable degradation is observed in the three consecutive cycles (Figure S23); the crystallinity and morphology are well maintained, and no Ru nanoparticle is discernible in the TEM image after photocatalysis (Figures S24 and S25), suggesting the good stability and recyclability of Ru_1/UiO-67-*o*-$(NH_2)_2$.

To understand the activity variation in the photocatalytic hydrogen production over Ru_1/UiO-67-X, their photoelectrochemical properties have been measured. The steady-state photoluminescence (PL) emission spectra reveal that the introduction of Ru_1 sites and amino groups significantly improves the charge transfer in the MOF (Figures S26−S29). Ultraviolet−visible (UV−vis) spectra of UiO-67-X depict the light-harvesting capability trend of UiO-67-*m*-$(NH_2)_2$ > UiO-67-*o*-$(NH_2)_2$ > UiO-67 (Figure 3b). Accordingly, their Tauc plots display the reversed band gap sequence of UiO-67-*m*-$(NH_2)_2$ < UiO-67-*o*-$(NH_2)_2$ < UiO-67 (Figures S30−S32). These results reflect that the introduction of $-NH_2$ groups does improve light absorption. However, the unmatched tendency with the photocatalytic activity indicates that the light absorption capability is not the dominant factor for the different activity. Meanwhile, the lowest unoccupied molecular orbitals (LUMOs) of UiO-67-X, obtained from Mott−Schottky measurements, are all negative than the H_2O reduction potential (−0.4 V vs NHE, pH = 6.8), demonstrat-

https://doi.org/10.1021/jacs.4c06013
J. Am. Chem. Soc. 2024, 146, 20391−20400

ing the thermodynamic feasibility of hydrogen generation by visible light photocatalysis (Figures S33−S35).[39,40] In addition, the photocurrent responses show the order of Ru_1/UiO-67-*o*-$(NH_2)_2$ > Ru_1/UiO-67-*m*-$(NH_2)_2$ > Ru_1/UiO-67 (Figure 3c), indicating that the behaviors of electron−hole separation and charge transfer are consistent with the photocatalytic hydrogen production rate. Similarly, electrochemical impedance spectroscopy (EIS) shows that the tendency of Nyquist plot radii is Ru_1/UiO-67 > Ru_1/UiO-67-*m*-$(NH_2)_2$ > Ru_1/UiO-67-*o*-$(NH_2)_2$ (Figure 3d). Therefore, the primary cause for the activity difference might be the introduction of amino groups that gives rise to an enhanced charge separation efficiency and a reduced charge transfer resistance. Moreover, the closer the proximity between the $-NH_2$ group and Ru_1 sites, the higher is the photocatalytic H_2 production activity observed.

The roles of $-NH_2$ groups around the Ru_1 sites in photocatalytic H_2 production have been further decoded. Generally, the $-NH_2$ groups could interact with H_2O molecules through hydrogen bonds, suggesting that the incorporation of $-NH_2$ groups is likely to improve water adsorption of resulting catalysts.[41,42] To prove this, the source of hydrogen produced in the photocatalytic reaction is identified by mass spectrometry (MS). The results declare that only H_2 (m/z = 2) is detected when H_2O is used in the photocatalytic system, while D_2 (m/z = 4) becomes the major product when H_2O is substituted with D_2O (Figures 4a,b and S36), demonstrating that water should be the dominant hydrogen source. The water vapor adsorption profiles of Ru_1/UiO-67-*o*-$(NH_2)_2$ and Ru_1/UiO-67-*m*-$(NH_2)_2$ display a similar high adsorption amount with Type IV isotherms at 298 K, showcasing a significantly higher adsorption capacity than Ru_1/UiO-67 in the absence of the $-NH_2$ group at P/P_0 = 0.91 (Figure 4c). The difference of water vapor adsorption isotherms between Ru_1/UiO-67-*o*-$(NH_2)_2$ and Ru_1/UiO-67-*m*-$(NH_2)_2$ may be attributed to the closer proximity of $-NH_2$ groups and Zr-oxo clusters in Ru_1/UiO-67-*o*-$(NH_2)_2$. This closer proximity gives greater steric hindrance, leading to a slightly slower adsorption kinetics. Compared to the adsorption plots, the noticeable hysteresis observed in the desorption plots may be attributed to irreversible capillary condensation and the interactions between the adsorbed water molecules and the binding sites.[43] Meanwhile, density functional theory (DFT) calculations illustrate that the adsorption energies for one water molecule adsorbed on Ru_1/UiO-67-*o*-$(NH_2)_2$, Ru_1/UiO-67-*m*-$(NH_2)_2$, and Ru_1/UiO-67 are −0.458, −0.454, and −0.344 eV, respectively (Figure S37). The experimental and computational results jointly demonstrate that the presence of amino groups improves the water adsorption capability of Ru_1/UiO-67-X. The increased concentration of the substrate (H_2O molecule) caused by the introduction of the $-NH_2$ group in the photocatalysts would be definitely favorable to the H_2 production activity.

Specific peaks at around 3449 and 3670 cm^{-1}, attributed to the water molecules and −OH groups on Zr-oxo clusters, respectively, are observed in DRIFTS spectra recording water adsorption on UiO-67 (Figure S38).[30,44,45] Time-dependent water adsorption and desorption experiments for UiO-67 further confirm the weak interactions between the −OH groups and water molecules (Figure S39),[46] which is observed in UiO-67-*m*-$(NH_2)_2$ and UiO-67-*o*-$(NH_2)_2$ as well (Figure S40). Moreover, the vibrational peaks corresponding to the $-NH_2$ groups in UiO-67-*o*-$(NH_2)_2$ and UiO-67-*m*-$(NH_2)_2$ significantly decrease with the addition of water (Figures 4d and S41a). These peaks progressively re-emerge when water is removed through purging with Ar gas (Figures 4e and S41b). Meanwhile, the ^1H NMR results indicate that the chemical shifts of the active hydrogen atoms from the $-NH_2$ groups on UiO-67-*o*-$(NH_2)_2$ and UiO-67-*m*-$(NH_2)_2$ gradually blue-shift with the increased amount of introduced water (Figures S42 and S43).[47,48] Given the alteration in the chemical shift signifies a modification in the electronic surroundings of the active hydrogen atoms within $-NH_2$ groups, which is obviously attributed to the formation of hydrogen bonds between the $-NH_2$ groups and water molecules.[49]

To further investigate the reason behind the shift to a higher field for the active hydrogen atoms from the $-NH_2$ group, controlled experiments have been performed. When the nitrogen atoms in the $-NH_2$ group serve as proton acceptors in the hydrogen bonding (accepting a proton from benzyl alcohol), the active hydrogen atom within these groups exhibits a decreased chemical shift in ^1H NMR spectra (Figure S44). Conversely, when the $-NH_2$ group acts as a proton donor and forms hydrogen bonds with benzaldehyde, their active hydrogen atoms are characterized by an increased chemical shift (Figure S44). Consequently, the ^1H NMR spectra of active hydrogen atoms in $-NH_2$ groups showcasing a low chemical shift are attributed to their role as proton acceptors in the hydrogen bonding with H_2O. Overall, the above DRIFTS spectra for water adsorption and ^1H NMR data unambiguously demonstrate that the $-NH_2$ groups can form hydrogen bonds with water molecules, as observed in the previous study,[50] generating particular hydrogen-bonding microenvironment around Ru_1 sites, leading to an increased water adsorption capacity.

DFT calculations have been carried out to investigate the influence of the distance between the $-NH_2$ group and the Ru_1 sites on the photocatalytic activity. The optimal structure of Ru_1/UiO-67-X involving the H_2O molecule demonstrates that three short hydrogen bonds (O−H···O, O−H···N, and O−H···S) are formed between H_2O and Ru_1/UiO-67-*o*-$(NH_2)_2$, whereas only one long hydrogen bond (O−H···O) is generated between H_2O with Ru_1/UiO-67-*m*-$(NH_2)_2$ or Ru_1/UiO-67 (Figure S45). Furthermore, the crystal orbital Hamilton population (COHP) is employed to theoretically analyze the bonding strength of the H_2O molecule with Ru_1/UiO-67-X.[51] There are two O−H bonds for the water molecule around the Ru_1 site; for the O−H bond far from the Ru_1 sites, called O−H (far), on Ru_1/UiO-67-*o*-$(NH_2)_2$, a pronounced antibonding signal peak is observed near the Fermi level in the bonding energy area, indicating that electrons have occupied the antibonding orbital. This means that the bond is unstable and easy to break, implying that O−H (far) on Ru_1/UiO-67-*o*-$(NH_2)_2$ possesses a lower dissociation energy. Meanwhile, the integrated COHP under the Fermi level (-ICOHP) values of O−H (far) are 1.243, 1.353, and 1.368 eV on Ru_1/UiO-67-*o*-$(NH_2)_2$, Ru_1/UiO-67-*m*-$(NH_2)_2$, and Ru_1/UiO-67, respectively (Figure S46). The results reflect that the presence of the amino group can facilitate the dissociation of H_2O, and the very short distance between the $-NH_2$ group and the Ru_1 site gives rise to the lowest energy of H_2O dissociation in Ru_1/UiO-67-*o*-$(NH_2)_2$. In addition, for the O−H bond near the Ru_1 site, denoted as O−H (near), its -ICOHP value on Ru_1/UiO-67-X presents slight differences, with all values around 1.33 eV (Figure S47), indicating that their O−H dissociation abilities are similar and

https://doi.org/10.1021/jacs.4c06013
J. Am. Chem. Soc. 2024, 146, 20391−20400

undisturbed by the $-NH_2$ group. Overall, the computational results further verify that the neighboring $-NH_2$ groups' close proximity to the Ru_1 sites creates hydrogen-bonding microenvironment around Ru_1 sites, contributing to the acceleration of water splitting, which is the decisive factor for promoting photocatalytic hydrogen production.

CONCLUSIONS

In summary, single-atom Ru_1 sites are anchored onto the Zr-oxo clusters of UiO-67-X (X = -H, -*m*-$(NH_2)_2$, -*o*-$(NH_2)_2$), affording Ru_1/UiO-67-X, in which the distance between the Ru_1 site and the $-NH_2$ group can be precisely controlled for photocatalytic H_2 production. The $-NH_2$ group introduces hydrogen-bonding microenvironment around Ru_1 sites based on its hydrogen bonding with the substrate, the water molecule. Remarkably, Ru_1/UiO-67-*o*-$(NH_2)_2$, featuring hydrogen-bonding microenvironment in close proximity to the Ru_1 sites, exhibits a very high H_2 production rate up to 20.52 mmol g^{-1} h^{-1}, which has ∼4.6 and ∼146.6 times higher activity than that of Ru_1/UiO-67-*m*-$(NH_2)_2$ and Ru_1/UiO-67, respectively. Both experimental and theoretical results collectively indicate that the close distance between the hydrogen-bonding microenvironment and Ru_1 sites plays critical roles in boosting photocatalytic hydrogen production. This close proximity is favorable to charge transfer and facilitates H_2O dissociation, thereby significantly improving the activity. This study, for the first time, provides insights into how the hydrogen-bonding microenvironment around catalytic metal sites influences photocatalytic hydrogen production. This work opens a new avenue to the design and synthesis of efficient photocatalysts by introducing noncovalent interaction microenvironment around catalytic sites.

EXPERIMENTAL SECTION

Materials and Equipment. All chemicals were obtained from commercial suppliers and used without treatment, unless otherwise stated. The Rigaku Miniflex 600 X-ray diffractometer, featuring graphite-monochromatized Cu Kα radiation (λ = 1.54 Å), was employed for powder X-ray diffraction (XRD) pattern acquisition. Nitrogen sorption isotherms were measured using a Micromeritics ASAP 2020 at 77 K. The samples were activated at 150 °C for 12 h prior to the measurements. Scanning electron microscopy (SEM) images were captured using a Carl Zeiss Supra 40 SEM. Transmission electron microscopy (TEM) images were taken on a JEOL-2010 field emission microscope. The aberration-corrected high-angle annular dark-field scanning transmission electron microscopy (HAADF-STEM) image was obtained using Themis Z. The Talos F200X instrument, equipped with a Super-X EDX detector and operating at 200 kV, was utilized for HAADF-STEM and energy-dispersive X-ray spectroscopy (EDS) mapping analyses. The Ru content in the samples was quantified using an Optima 7300 DV inductively coupled plasma atomic emission spectrometer (ICP-AES). The ^1H nuclear magnetic resonance (NMR) spectra were recorded on a 400 MHz Bruker AC-400FT spectrometer. X-ray photoelectron spectroscopy (XPS) analysis was conducted on an ESCALAB 250 X-ray photoelectron spectrometer using monochromatized Al Kα radiation. The steady-state photoluminescence (PL) spectra were measured using a Hitachi FL-4600 fluorescence spectrometer with the excitation wavelength at 320 nm. For the PL measurements, 2 mg of the catalyst was dispersed ultrasonically in 6 mL of H_2O. The mass spectra (MS) were carried out using a Hiden HPR40 differential electrochemical mass spectrometry (DEMS) system equipped with a gas inlet detector. All species employed an ionization energy of 70 eV alongside an emission current of 1000 μA. The rate of hydrogen production was determined using a gas chromatograph (GC, Shimadzu 2014) equipped with a thermal conductivity detector (TCD) and using argon as the carrier gas. X-ray absorption spectroscopy (XAS) analyses of all samples were conducted at the station of BL14W1 of the Shanghai Synchrotron Radiation Facility (SSRF) and data were analyzed using the Athena and Artemis software packages. Water vapor adsorption kinetics were obtained using a BSD-VVS (vacuum vapor sorption) gravimetric analyzer [Beishide Instrument Technology (Beijing) Co., Ltd.] under a constant humidified airflow at 25 °C.

Synthesis of UiO-67. UiO-67 was synthesized from the reported literature with modifications.[34] Typically, 150 mg of $ZrCl_4$, 156 mg of 4,4′-biphenyldicarboxylic acid (H_2BPDC), 10 mL of DMF, 1.85 mL of acetic acid (CH_3COOH), and 0.75 mL of deionized water were added to a 50 mL round-bottomed flask. Upon ultrasonic dissolution, the mixture was stirred at 120 °C for 30 min in an oil bath. After cooling down to room temperature, the product was washed three times with DMF and acetone.

Synthesis of UiO-67-*m*-$(NH_2)_2$. UiO-67-*m*-$(NH_2)_2$ was synthesized from the reported literature with modifications.[34] Typically, 150 mg of $ZrCl_4$, 39 mg of H_2BPDC, 131.6 mg of H_2BPDC-*m*-$(NH_2)_2$, 10 mL of DMF, 1.85 mL of CH_3COOH, and 0.75 mL of deionized water were added to a 50 mL round-bottomed flask. Upon ultrasonic dissolution, the mixture was stirred at 120 °C for 30 min in an oil bath. After cooling down to room temperature, the product was washed three times with DMF and acetone.

Synthesis of UiO-67-*o*-$(NH_2)_2$. UiO-67-*o*-$(NH_2)_2$ was synthesized from the reported literature with modifications.[34] Typically, 150 mg of $ZrCl_4$, 78 mg of H_2BPDC, 87.7 mg of H_2BPDC-*o*-$(NH_2)_2$, 10 mL of DMF, 1.85 mL of CH_3COOH, and 0.75 mL of deionized water were added to a 50 mL round-bottomed flask. Upon ultrasonic dissolution, the mixture was stirred at 120 °C for 30 min in an oil bath. After cooling down to room temperature, the product was washed three times with DMF and acetone.

Synthesis of Ru_1/UiO-67-X (X = -H, -*m*-$(NH_2)_2$, -*o*-$(NH_2)_2$). Typically, 100 mg of UiO-67-X (X = -H, -*m*-$(NH_2)_2$, -*o*-$(NH_2)_2$) and 2.5 mg of $RuCl_3$ were added to a 10 mL microwave vessel, followed by the addition of 4 mL of acetonitrile. The mixture underwent ultrasonic dispersion before being rapidly heated to 85 °C using microwave assistance, where it was maintained with continuous stirring for 30 min. After cooling down to ambient temperature, the solid product was isolated through centrifugation and subjected to three successive washes with DMF and acetone. After drying at 85 °C in an oven, 100 mg of the sample obtained above and 200 mg of thioacetamide were added to 4 mL of DMF. The mixture was then stirred at 120 °C for 1 h under nitrogen protection. After cooling to room temperature, the sample was washed three times with DMF and acetone, respectively, and dried under vacuum at room temperature.

Photoelectrochemical Measurements. Photocurrent measurements were conducted using a CHI760E electrochemical workstation (Chenhua Instrument, Shanghai, China) within a conventional three-electrode system. For these experiments, 2 mg of the photocatalyst was dispersed in a solution containing 1 mL of ethanol and 10 μL of 5 wt % Nafion solution. The working electrode was prepared by applying a 60 μL aliquot of this mixture onto the surface of an indium tin oxide (ITO) plate, covering an area of 2 cm^2. A platinum plate served as the counter electrode, while an Ag/AgCl electrode was utilized as the reference electrode. The electrolyte solution consisted of 0.1 M Na_2SO_4. Visible light irradiation was provided by a 300 W xenon lamp equipped with a cutoff filter (λ > 380 nm). Photocurrent responses were recorded under intermittent illumination, with a bias potential of +0.5 V applied to the samples. The EIS and Mott–Schottky plot measurements were carried out using a Zahner Zennium electrochemical workstation, set up with a standard three-electrode configuration. In a typical preparation, 3 mg of the photocatalysts were dispersed in a mixture containing 10 μL of 5 wt % Nafion and 1 mL of ethanol. This mixture was then applied (20 μL) onto a glassy carbon electrode (Φ = 3 cm) to serve as the working electrode. A platinum plate and an Ag/AgCl electrode were employed as the counter and reference electrodes, respectively. The electrolyte solution consisted of 0.1 M Na_2SO_4. The EIS measurements were conducted at a fixed bias potential of −1.5 V under visible light

https://doi.org/10.1021/jacs.4c06013
J. Am. Chem. Soc. 2024, 146, 20391−20400

irradiation (λ > 380 nm). The Mott−Schottky plots were obtained at frequencies of 1000, 2000, and 3000 Hz.

Photocatalytic Hydrogen Production. Photocatalytic hydrogen production was carried out in a 160 mL optical reaction vessel (Beijing Perfectlight Technology Co., Ltd., China) at room temperature with continuous stirring. Typically, 5 mg of the photocatalyst was suspended in a solvent mixture consisting of 18 mL of acetonitrile, 2 mL of triethylamine (TEA), and 0.2 mL of deionized water, unless otherwise stated. The mixture was thoroughly mixed to achieve a homogeneous suspension, which was then stirred and purged with nitrogen for approximately 10 min to remove the air. Visible light irradiation was provided by a 300 W xenon lamp, fitted with a UV cutoff filter (λ > 380 nm). Circulating water was used throughout the reaction to maintain a steady temperature of approximately 25 °C. To measure hydrogen production, 200 μL samples of the headspace were periodically withdrawn and analyzed using a gas chromatograph (Shimadzu GC-2014 with argon as the carrier gas) equipped with a thermal conductivity detector (TCD). The hydrogen concentration was determined using a calibration curve based on an internal hydrogen standard.

DRIFTS Spectrum Measurements. The diffuse reflectance infrared Fourier transform spectroscopy (DRIFTS) spectra for CO adsorption were acquired using a Nicolet iS10 spectrometer equipped with a MCT detector. The typical procedure involved heating the samples first to 120 °C for 30 min under an argon gas purge. This step was essential for removing any water from the sample surfaces. Once the samples were cooled down to ambient temperature, a background signal was recorded at room temperature. Subsequently, CO gas was let in and the DRIFTS spectra for CO adsorption were taken in the range of 4000−1100 cm^{-1}, continuing until the point of CO adsorption saturation was reached. To obtain the final chemisorption of the CO signal spectra, any physically adsorbed CO was purged away from the samples using argon gas. The typical procedure for collecting the DRIFTS spectra of H_2O adsorption and desorption was conducted using the Nicolet iS10 spectrometer. Initially, the sample was heated to 120 °C under an argon gas purge and maintained at this temperature for 30 min to remove H_2O from the MOF pores. After cooling down to room temperature, the background signal was recorded. Subsequently, the sample was treated with argon gas carrying H_2O to introduce moisture into the samples, with the spectra being collected every 5 min for a duration of 45 min. Finally, the samples were purged with argon gas to remove H_2O, and the signals were recorded at 5 min intervals for another 45 min.

Computational Details. DFT calculations were performed using the Vienna *ab initio* simulation package (VASP).[52,53] The generalized gradient approximation (GGA) of the Perdew−Burke−Ernzerhof (PBE) form was used to describe the exchange−correlation functional,[54] while the projector-augmented wave (PAW) potentials were employed to illustrate the electron−ion interactions.[55,56] The van der Waals interactions were described by using the DFT-D3 (BJ) method.[57] Coulomb and exchange interactions were adjusted by using the PBE + U method, with U = 4.0 and 3.0 eV for the 4d orbital of Zr and Ru, respectively.[58,59] A single Γ-center k-point grid was performed using spin polarization in all calculations. The convergence criteria for self-consistent energy and Hellmann−Feynman force were 10^{-5} eV and 0.03 eV $Å^{-1}$, respectively, with a plane-wave cutoff energy of 520 eV. The crystal orbital Hamilton population (COHP) analysis was performed using Lobster.[60]

■ ASSOCIATED CONTENT

Supporting Information

The Supporting Information is available free of charge at https://pubs.acs.org/doi/10.1021/jacs.4c06013.

Additional details on the synthesis of ligands; characterization data; ^{1}H NMR spectra; SEM; TEM; and HAADF-STEM images; XPS spectra; PL emission spectra; Mott−Schottky plots; amount of Ru species loaded into Ru_1/UiO-67-X based on ICP-AES results (PDF)

■ AUTHOR INFORMATION

Corresponding Author

Hai-Long Jiang − *Hefei National Research Center for Physical Sciences at the Microscale, Department of Chemistry, University of Science and Technology of China, Hefei, Anhui 230026, P. R. China;* orcid.org/0000-0002-2975-7977; Email: jianglab@ustc.edu.cn

Authors

Shuaishuai Hu − *Hefei National Research Center for Physical Sciences at the Microscale, Department of Chemistry, University of Science and Technology of China, Hefei, Anhui 230026, P. R. China*

Ming-Liang Gao − *Hefei National Research Center for Physical Sciences at the Microscale, Department of Chemistry, University of Science and Technology of China, Hefei, Anhui 230026, P. R. China*

Jiajia Huang − *Hefei National Research Center for Physical Sciences at the Microscale, Department of Chemistry, University of Science and Technology of China, Hefei, Anhui 230026, P. R. China*

He Wang − *Hefei National Research Center for Physical Sciences at the Microscale, Department of Chemistry, University of Science and Technology of China, Hefei, Anhui 230026, P. R. China*

Qingyu Wang − *Hefei National Research Center for Physical Sciences at the Microscale, Department of Chemistry, University of Science and Technology of China, Hefei, Anhui 230026, P. R. China; National Synchrotron Radiation Laboratory, University of Science and Technology of China, Hefei, Anhui 230029, P. R. China*

Weijie Yang − *School of Energy and Power Engineering, North China Electric Power University, Baoding, Hebei 071003, P. R. China;* orcid.org/0000-0002-0232-1129

Zhihu Sun − *National Synchrotron Radiation Laboratory, University of Science and Technology of China, Hefei, Anhui 230029, P. R. China;* orcid.org/0000-0002-3898-969X

Xusheng Zheng − *National Synchrotron Radiation Laboratory, University of Science and Technology of China, Hefei, Anhui 230029, P. R. China;* orcid.org/0000-0003-2559-6106

Complete contact information is available at: https://pubs.acs.org/10.1021/jacs.4c06013

Author Contributions

All authors have concurred with the final version of the manuscript.

Notes

The authors declare no competing financial interest.

■ ACKNOWLEDGMENTS

This project was supported by the National Key Research and Development Program of China (2021YFA1500402), the National Natural Science Foundation of China (22331009, 22101269), the Strategic Priority Research Program of the Chinese Academy of Sciences (XDB0450302, XDB0540000), the Fundamental Research Funds for the Central Universities (WK2060000038), and the Postdoctoral Fellowship Program of CPSF (GZC20232532). We thank the BL14W1 station at

SSRF for their support in conducting XAFS measurements. We thank the supercomputing center at the University of Science and Technology of China (USTC) and the Hefei Advanced Computing Center for providing computational resources. This work was partially carried out at the Instruments Center for Physical Science, USTC.

REFERENCES

(1) Sang, R.; Wei, Z.; Hu, Y.; Alberico, E.; Wei, D.; Tian, X.; Ryabchuk, P.; Spannenberg, A.; Razzaq, R.; Jackstell, R.; Massa, J.; Sponholz, P.; Jiao, H.; Junge, H.; Beller, M. Methyl formate as a hydrogen energy carrier. *Nat. Catal.* **2023**, *6*, 543−550.
(2) Lin, L.; Zhou, W.; Gao, R.; Yao, S.; Zhang, X.; Xu, W.; Zheng, S.; Jiang, Z.; Yu, Q.; Li, Y.-W.; Shi, C.; Wen, X.-D.; Ma, D. Low-temperature hydrogen production from water and methanol using Pt/α-MoC catalysts. *Nature* **2017**, *544*, 80−83.
(3) Reece, S. Y.; Hamel, J. A.; Sung, K.; Jarvi, T. D.; Esswein, A. J.; Pijpers, J. J. H.; Nocera, D. G. Wireless solar water splitting using silicon-based semiconductors and earth-abundant catalysts. *Science* **2011**, *334*, 645−648.
(4) Xiao, J.; Hisatomi, T.; Domen, K. Narrow-band-gap particulate photocatalysts for one-step-excitation overall water splitting. *Acc. Chem. Res.* **2023**, *56*, 878−888.
(5) Li, Z.; Li, R.; Jing, H.; Xiao, J.; Xie, H.; Hong, F.; Ta, N.; Zhang, X.; Zhu, J.; Li, C. Blocking the reverse reactions of overall water splitting on a Rh/GaN−ZnO photocatalyst modified with Al_2O_3. *Nat. Catal.* **2023**, *6*, 80−88.
(6) Liu, L.; Du, S.; Guo, X.; Xiao, Y.; Yin, Z.; Yang, N.; Bao, Y.; Zhu, X.; Jin, S.; Feng, Z.; Zhang, F. Water-stable nickel metal-organic framework nanobelts for cocatalyst-free photocatalytic water splitting to produce hydrogen. *J. Am. Chem. Soc.* **2022**, *144*, 2747−2754.
(7) Bhattacharjee, S.; Linley, S.; Reisner, E. Solar reforming as an emerging technology for circular chemical industries. *Nat. Rev. Chem.* **2024**, *8*, 87−105.
(8) Liu, M.; Zhang, G.; Liang, X.; Pan, Z.; Zheng, D.; Wang, S.; Yu, Z.; Hou, Y.; Wang, X. Rh/Cr_2O_3 and CoO_x cocatalysts for efficient photocatalytic water splitting by poly (triazine imide) crystals. *Angew. Chem., Int. Ed.* **2023**, *62*, No. e202304694, DOI: 10.1002/anie.202304694.
(9) Wu, X.; Zhang, H.; Dong, J.; Qiu, M.; Kong, J.; Zhang, Y.; Li, Y.; Xu, G.; Zhang, J.; Ye, J. Surface step decoration of isolated atom as electron pumping: Atomic-level insights into visible-light hydrogen evolution. *Nano Energy* **2018**, *45*, 109−117.
(10) Thangamuthu, M.; Vankayala, K.; Xiong, L.; Conroy, S.; Zhang, X.; Tang, J. Tungsten oxide-based Z-scheme for visible light-driven hydrogen production from water splitting. *ACS Catal.* **2023**, *13*, 9113−9124.
(11) Huang, W.; Su, C.; Zhu, C.; Bo, T.; Zuo, S.; Zhou, W.; Ren, Y.; Zhang, Y.; Zhang, J.; Rueping, M.; Zhang, H. Isolated electron trap-induced charge accumulation for efficient photocatalytic hydrogen production. *Angew. Chem., Int. Ed.* **2023**, *62*, No. e202304634.
(12) Yang, Y.; Chu, X.; Zhang, H.-Y.; Zhang, R.; Liu, Y.-H.; Zhang, F.-M.; Lu, M.; Yang, Z.-D.; Lan, Y.-Q. Engineering β-ketoamine covalent organic frameworks for photocatalytic overall water splitting. *Nat. Commun.* **2023**, *14*, No. 593.
(13) Lan, G.; Fan, Y.; Shi, W.; You, E.; Veroneau, S. S.; Lin, W. Biomimetic active sites on monolayered metal-organic frameworks for artificial photosynthesis. *Nat. Catal.* **2022**, *5*, 1006−1018.
(14) Xu, W.; Wu, Y.; Gu, W.; Du, D.; Lin, Y.; Zhu, C. Atomic-level design of metalloenzyme-like active pockets in metal−organic frameworks for bioinspired catalysis. *Chem. Soc. Rev.* **2024**, *53*, 137−162.
(15) Furukawa, H.; Cordova, K. E.; O'Keeffe, M.; Yaghi, O. M. The chemistry and applications of metal-organic frameworks. *Science* **2013**, *341*, No. 1230444.
(16) Zhou, H.-C. J.; Kitagawa, S. Metal-organic frameworks (MOFs). *Chem. Soc. Rev.* **2014**, *43*, 5415−5418.
(17) Zhao, X.; Wang, Y.; Li, D. S.; Bu, X.; Feng, P. Metal-organic frameworks for separation. *Adv. Mater.* **2018**, *30*, No. 1705189.
(18) Jiao, L.; Jiang, H.-L. Metal-organic frameworks for catalysis: Fundamentals and future prospects. *Chin. J. Catal.* **2023**, *45*, 1−5, DOI: 10.1016/S1872-2067(22)64193-7.
(19) Lin, R.-B.; Zhang, Z.; Chen, B. Achieving high performance metal-organic framework materials through pore engineering. *Acc. Chem. Res.* **2021**, *54*, 3362−3376.
(20) Li, G.; Zhao, S.; Zhang, Y.; Tang, Z. Metal-organic frameworks encapsulating active nanoparticles as emerging composites for catalysis: Recent progress and perspectives. *Adv. Mater.* **2018**, *30*, No. 1800702.
(21) Wei, Y.-S.; Zhang, M.; Zou, R.; Xu, Q. Metal-organic framework-based catalysts with single metal sites. *Chem. Rev.* **2020**, *120*, 12089−12174.
(22) Dhakshinamoorthy, A.; Li, Z.; Yang, S.; García, H. Metal-organic framework heterojunctions for photocatalysis. *Chem. Soc. Rev.* **2024**, *53*, 3002−3035.
(23) Hu, H.; Wang, Z.; Cao, L.; Zeng, L.; Zhang, C.; Lin, W.; Wang, C. Metal-organic frameworks embedded in a liposome facilitate overall photocatalytic water splitting. *Nat. Chem.* **2021**, *13*, 358−366.
(24) Yang, W.; Wang, H. J.; Liu, R. R.; Wang, J. W.; Zhang, C.; Li, C.; Zhong, D. C.; Lu, T. B. Tailoring crystal facets of metal-organic layers to enhance photocatalytic activity for CO_2 reduction. *Angew. Chem., Int. Ed.* **2021**, *60*, 409−414.
(25) Lerma-Berlanga, B.; Ganivet, C. R.; Almora-Barrios, N.; Tatay, S.; Peng, Y.; Albero, J.; Fabelo, O.; González-Platas, J.; García, H.; Padial, N. M.; Martí-Gastaldo, C. Effect of linker distribution in the photocatalytic activity of multivariate mesoporous crystals. *J. Am. Chem. Soc.* **2021**, *143*, 1798−1806, DOI: 10.1021/jacs.0c09015.
(26) Nguyen, H. L. Metal-organic frameworks for photocatalytic water splitting. *Sol. RRL* **2021**, *5*, No. 2100198.
(27) Manna, K.; Ji, P.; Lin, Z.; Greene, F. X.; Urban, A.; Thacker, N. C.; Lin, W. Chemoselective single-site earth-abundant metal catalysts at metal-organic framework nodes. *Nat. Commun.* **2016**, *7*, No. 12610.
(28) Khoo, R. S. H.; Fiankor, C.; Yang, S.; Hu, W.; Yang, C.; Lu, J.; Morton, M. D.; Zhang, X.; Liu, Y.; Huang, J.; Zhang, J. Postsynthetic modification of the nonanuclear node in a zirconium metal-organic framework for photocatalytic oxidation of hydrocarbons. *J. Am. Chem. Soc.* **2023**, *145*, 24052−24060.
(29) Abdel-Mageed, A. M.; Rungtaweevoranit, B.; Parlinska-Wojtan, M.; Pei, X.; Yaghi, O. M.; Behm, R. J. Highly active and stable single-atom Cu catalysts supported by a metal-organic framework. *J. Am. Chem. Soc.* **2019**, *141*, 5201−5210.
(30) Ma, X.; Liu, H.; Yang, W.; Mao, G.; Zheng, L.; Jiang, H.-L. Modulating coordination environment of single-atom catalysts and their proximity to photosensitive units for boosting MOF photocatalysis. *J. Am. Chem. Soc.* **2021**, *143*, 12220−12229.
(31) Liu, J.; Goetjen, T. A.; Wang, Q.; Knapp, J. G.; Wasson, M. C.; Yang, Y.; Syed, Z. H.; Delferro, M.; Notestein, J. M.; Farha, O. K.; Hupp, J. T. MOF-enabled confinement and related effects for chemical catalyst presentation and utilization. *Chem. Soc. Rev.* **2022**, *51*, 1045−1097.
(32) Kim, D.; Kang, M.; Ha, H.; Hong, C. S.; Kim, M. Multiple functional groups in metal-organic frameworks and their positional regioisomerism. *Coord. Chem. Rev.* **2021**, *438*, No. 213892.
(33) Cavka, J. H.; Jakobsen, S.; Olsbye, U.; Guillou, N.; Lamberti, C.; Bordiga, S.; Lillerud, K. P. A new zirconium inorganic building brick forming metal organic frameworks with exceptional stability. *J. Am. Chem. Soc.* **2008**, *130*, 13850−13851.
(34) He, T.; Xu, X.; Ni, B.; Wang, H.; Long, Y.; Hu, W.; Wang, X. Fast and scalable synthesis of uniform zirconium-, hafnium-based metal-organic framework nanocrystals. *Nanoscale* **2017**, *9*, 19209−19215.
(35) Yang, G.; Wang, D.; Wang, Y.; Hu, W.; Hu, S.; Jiang, J.; Huang, J.; Jiang, H.-L. Modulating the primary and secondary coordination spheres of single Ni(II) sites in metal-organic frameworks for boosting photocatalysis. *J. Am. Chem. Soc.* **2024**, *146*, 10798−10805.

(36) Ren, G.; Zhao, J.; Zhao, Z.; Li, Z.; Wang, L.; Zhang, Z.; Li, C.; Meng, X. Defects-induced single-atom anchoring on metal-organic frameworks for high-efficiency photocatalytic nitrogen reduction. *Angew. Chem., Int. Ed.* **2024**, *63*, No. e202314408.
(37) Fang, G.; Wei, F.; Lin, J.; Zhou, Y.; Sun, L.; Shang, X.; Lin, S.; Wang, X. Retrofitting Zr-oxo nodes of UiO-66 by Ru single atoms to boost methane hydroxylation with nearly total selectivity. *J. Am. Chem. Soc.* **2023**, *145*, 13169−13180.
(38) Escobar-Bedia, F. J.; Lopez-Haro, M.; Calvino, J. J.; Martin-Diaconescu, V.; Simonelli, L.; Perez-Dieste, V.; Sabater, M. J.; Concepción, P.; Corma, A. Active and regioselective Ru single-site heterogeneous catalysts for alpha-olefin hydroformylation. *ACS Catal.* **2022**, *12*, 4182−4193.
(39) Xu, M.; Li, D.; Sun, K.; Jiao, L.; Xie, C.; Ding, C.; Jiang, H.-L. Interfacial microenvironment modulation boosting electron transfer between metal nanoparticles and MOFs for enhanced photocatalysis. *Angew. Chem., Int. Ed.* **2021**, *60*, 16372−16376.
(40) Lin, X. C.; Wang, Y. M.; Chen, X.; You, P. Y.; Mo, K. M.; Ning, G. H.; Li, D. A photosensitizing metal-organic framework as a tandem reaction catalyst for primary alcohols from terminal alkenes and alkynes. *Angew. Chem., Int. Ed.* **2023**, *62*, No. e202306497, DOI: 10.1002/anie.202306497.
(41) Zhu, N. X.; Wei, Z. W.; Chen, C. X.; Xiong, X. H.; Xiong, Y. Y.; Zeng, Z.; Wang, W.; Jiang, J. J.; Fan, Y. N.; Su, C. Y. High water adsorption MOFs with optimized pore-nanospaces for autonomous indoor humidity control and pollutants removal. *Angew. Chem., Int. Ed.* **2021**, *61*, No. e202112097, DOI: 10.1002/anie.202112097.
(42) Shi, Z.; Tao, Y.; Wu, J.; Zhang, C.; He, H.; Long, L.; Lee, Y.; Li, T.; Zhang, Y.-B. Robust metal-triazolate frameworks for CO_2 capture from flue gas. *J. Am. Chem. Soc.* **2020**, *142*, 2750−2754.
(43) Kalmutzki, M. J.; Diercks, C. S.; Yaghi, O. M. Metal-organic frameworks for water harvesting from air. *Adv. Mater.* **2018**, *30* (37), No. 1704304.
(44) Chen, F.; Wang, J.; Yang, S.; Jiang, S.; Sun, C.; Song, S. Activating main-group Mg atomic sites within tri-s-triazine for photocatalytic H_2O overall splitting: Dynamic mechanism and performance. *ACS Catal.* **2023**, *13*, 5678−5688.
(45) Guo, W.; Chen, J.; Sun, S.; Zhou, Q. Investigation of water diffusion in hydrogel pore-filled membrane via 2D correlation time-dependent ATR-FTIR spectroscopy. *J. Mol. Struct.* **2018**, *1171*, 600−604.
(46) Planas, N.; Mondloch, J. E.; Tussupbayev, S.; Borycz, J.; Gagliardi, L.; Hupp, J. T.; Farha, O. K.; Cramer, C. J. Defining the proton topology of the Zr_6-based metal-organic framework NU-1000. *J. Phys. Chem. Lett.* **2014**, *5*, 3716−3723.
(47) Shi, S.; Yang, P.; Dun, C.; Zheng, W.; Urban, J. J.; Vlachos, D. G. Selective hydrogenation via precise hydrogen bond interactions on catalytic scaffolds. *Nat. Commun.* **2023**, *14*, No. 429.
(48) Shanahan, J. P.; Szymczak, N. K. Hydrogen bonding to a dinitrogen complex at room temperature: Impacts on N_2 activation. *J. Am. Chem. Soc.* **2019**, *141*, 8550−8556.
(49) Zhou, L.; Tian, S.; Du, X.; Liu, T.; Zhang, H.; Zhang, J.; Hu, S.; Chen, Z.; Zhang, J.; Cui, G. Suppressing hydrogen evolution in aqueous lithium-ion batteries with double-site hydrogen bonding. *ACS Energy Lett.* **2023**, *8*, 40−47.
(50) Islamoglu, T.; Ortuño, M. A.; Proussaloglou, E.; Howarth, A. J.; Vermeulen, N. A.; Atilgan, A.; Asiri, A. M.; Cramer, C. J.; Farha, O. K. Presence versus proximity: The role of pendant amines in the catalytic hydrolysis of a nerve agent simulant. *Angew. Chem., Int. Ed.* **2018**, *57*, 1949−1953.
(51) Wen, Q.; Duan, J.; Wang, W.; Huang, D.; Liu, Y.; Shi, Y.; Fang, J.; Nie, A.; Li, H.; Zhai, T. Engineering a local free water enriched microenvironment for surpassing platinum hydrogen evolution activity. *Angew. Chem., Int. Ed.* **2022**, *61*, No. e202206077.
(52) Kresse, G.; Furthmüller, J. Efficiency of ab-initio total energy calculations for metals and semiconductors using a plane-wave basis set. *Comput. Mater. Sci.* **1996**, *6*, 15−50.
(53) Kresse, G.; Furthmüller, J. Efficient iterative schemes for ab initio total-energy calculations using a plane-wave basis set. *Phys. Rev. B* **1996**, *54*, No. 11169, DOI: 10.1103/PhysRevB.54.11169.
(54) Perdew, J. P.; Burke, K.; Ernzerhof, M. Generalized gradient approximation made simple. *Phys. Rev. Lett.* **1996**, *77*, No. 3865, DOI: 10.1103/PhysRevLett.77.3865.
(55) Blöchl, P. E. Projector augmented-wave method. *Phys. Rev. B* **1994**, *50*, 17953−17979.
(56) Kresse, G.; Joubert, D. From ultrasoft pseudopotentials to the projector augmented-wave method. *Phys. Rev. B* **1999**, *59*, No. 1758, DOI: 10.1103/PhysRevB.59.1758.
(57) Grimme, S.; Ehrlich, S.; Goerigk, L. Effect of the damping function in dispersion corrected density functional theory. *J. Comput. Chem.* **2011**, *32*, 1456−1465.
(58) Puigdollers, A. R.; Illas, F.; Pacchioni, G. Structure and properties of zirconia nanoparticles from density functional theory calculations. *J. Phys. Chem. C* **2016**, *120*, 4392−4402.
(59) García-Mota, M.; Vojvodic, A.; Abild-Pedersen, F.; Nørskov, J. K. Electronic origin of the surface reactivity of transition-metal-doped TiO_2(110). *J. Phys. Chem. C* **2013**, *117*, 460−465.
(60) Nelson, R.; Ertural, C.; George, J.; Deringer, V. L.; Hautier, G.; Dronskowski, R. LOBSTER: Local orbital projections, atomic charges, and chemical-bonding analysis from projector-augmented-wave-based density-functional theory. *J. Comput. Chem.* **2020**, *41*, 1931−1940.

https://doi.org/10.1021/jacs.4c06013
J. Am. Chem. Soc. 2024, 146, 20391−20400